Supporting Information for

Block Copolymer Templated Synthesis of Core-Shell PtAu Bimetallic Nanocatalysts for the Methanol Oxidation Reaction

Kyle Mikkelsen,[†] Blake Cassidy,[†] Nicole Hofstetter,[†] Leah Bergquist,[†] Audrey Taylor[†] and David A. Rider[‡,†]*

[†] Department of Chemistry, Western Washington University,

516 High St., Bellingham WA 98225

[‡] Department of Engineering and Design, Western Washington University,

516 High St., Bellingham WA 98225

* To whom correspondence should be addressed: david.rider@wwu.edu

The FEI Tecnai Osiris TEM instrument was used for transmission electron microscopy and energy dispersive X-ray mapping. Calibration was performed using an automated procedure with a standardized Au-Pd grating. To ensure accuracy in the determination of lattice parameters, experimental samples were studied with the same imaging conditions as those for an Al calibration standard. Typically, the data images and/or diffraction pattern of an experimental samples are obtained followed by the study of the Al standard to the same electrical and magnetic conditions (i.e the same lens current or high voltage and positioning). Lattice parameters are assigned as per the below d-spacings for Al.

Miller Indices (hkl)	Lattice Spacing (Å)	Normalized Intensity	Lattice Constant (Å)
111	2.338	100	4.05
200	2.024	47	4.048
220	1.431	22	4.047
311	1.221	24	4.0489
222	1.169	7	4.0495
400	1.0124	2	4.0496
331	0.9289	8	4.049

Following the assignment of the d-spacings, a calibration constant (K) is calculated using the formula $K = S \times d$. K encompasses the wavelength of the electron beam, camera length and the associated variation in the crystallographic data, S represents the diameter of a diffraction ring in centimeters and d is the interplanar spacing in angstroms. The tolerance level for variation in the values for calibration constant for the first five lines is 1%. The imaging software is integrated with this calibration data to standardize the reciprocal readings of lattice spacing information acquired from FFT interpretations.
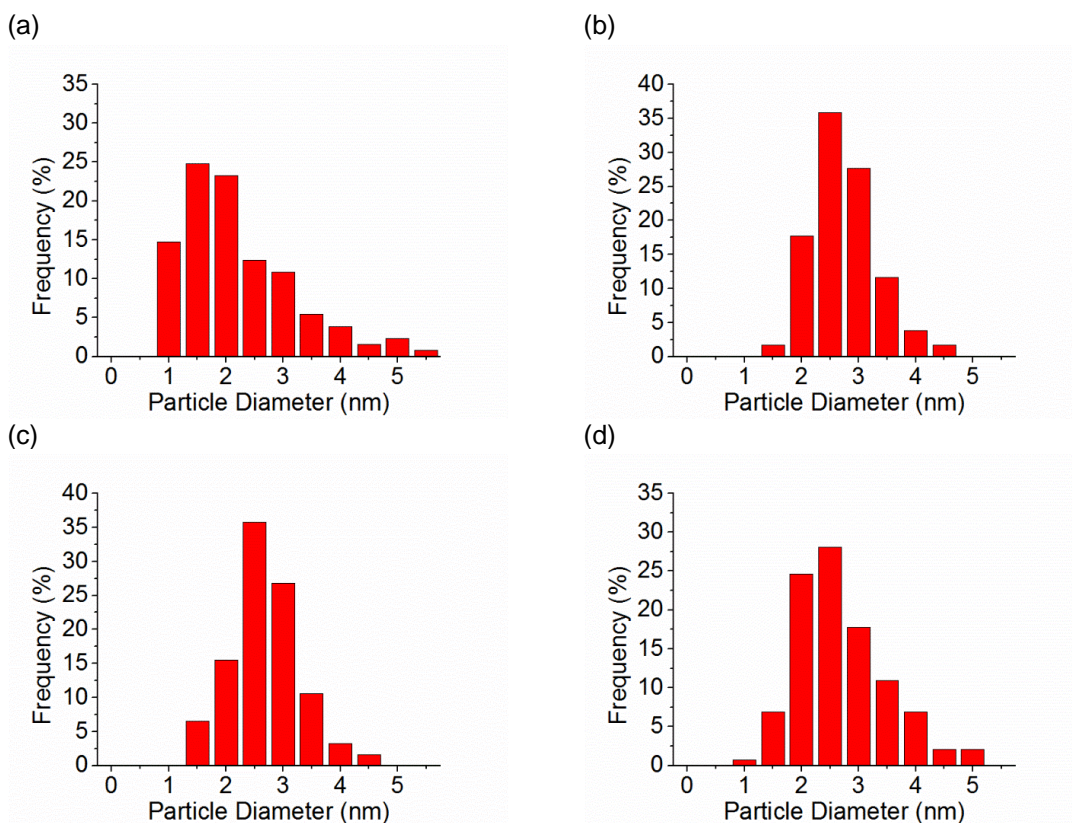
(a)

(b)

(c)

(d)

Figure S1. NP diameter histograms of: a) $Pt_{1.00}Au_{0.00}$ b) $Pt_{0.73}Au_{0.27}$ c) $Pt_{0.57}Au_{0.43}$ and d) $Pt_{0.49}Au_{0.51}$ synthesized from PS_{1392}-b-$P4VP_{471}$.
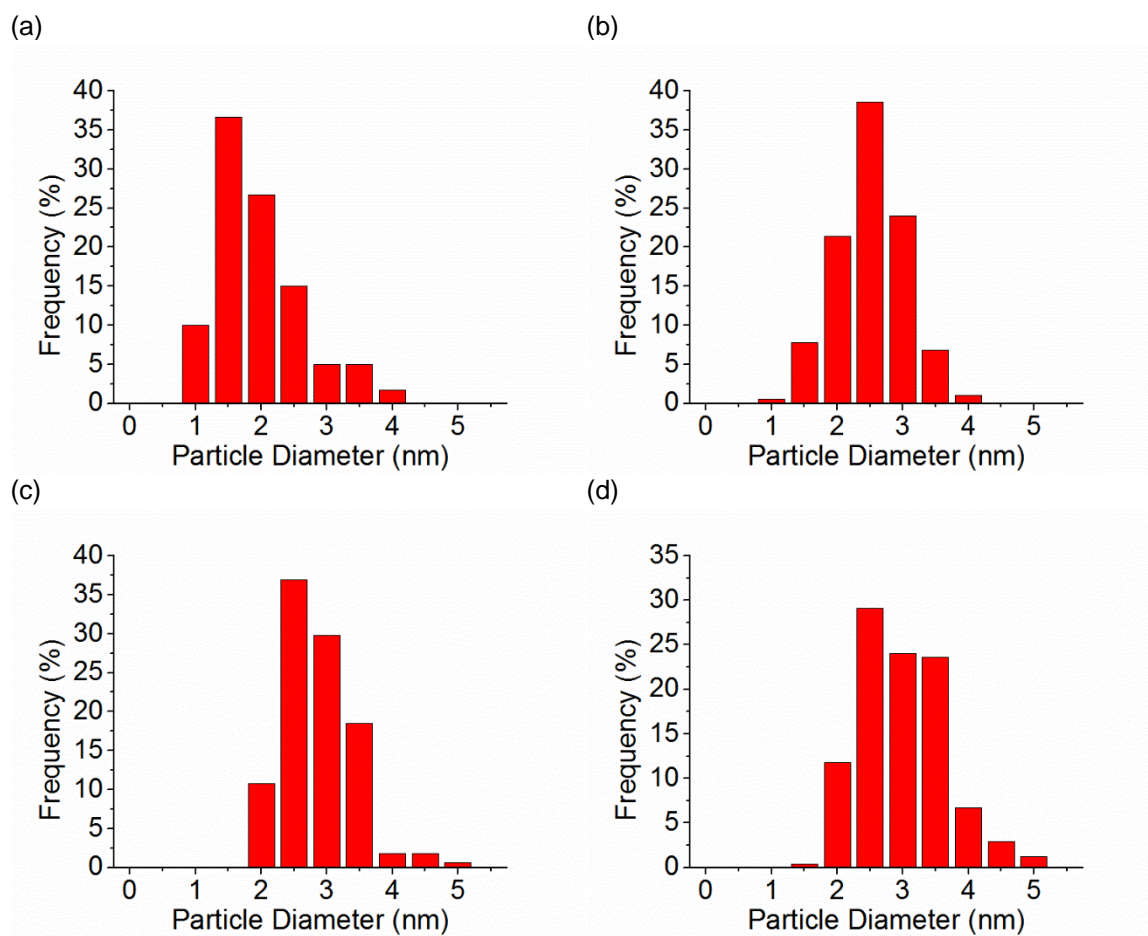
Figure S2. NP diameter histograms of: a) $Pt_{1.00}Au_{0.00}$ b) $Pt_{0.72}Au_{0.28}$ c) $Pt_{0.61}Au_{0.39}$ and d) $Pt_{0.56}Au_{0.44}$ synthesized from PS_{720}-b-$P4VP_{238}$.
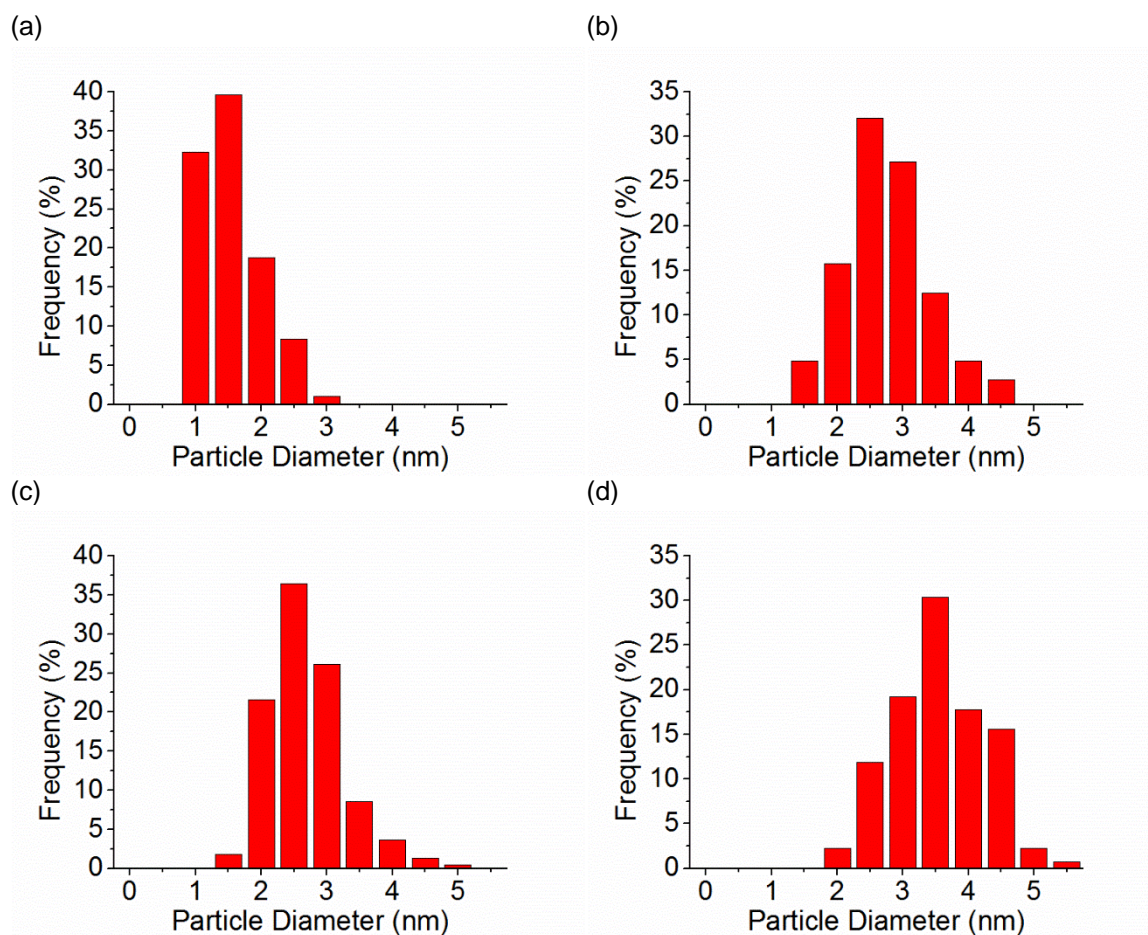
Figure S3. NP diameter histograms of: a) $Pt_{1.00}Au_{0.00}$ b) $Pt_{0.81}Au_{0.19}$ c) $Pt_{0.68}Au_{0.32}$ and d) $Pt_{0.61}Au_{0.39}$ synthesized from PS_{552}-*b*-$P4VP_{174}$.

(a)

(b)

(c)
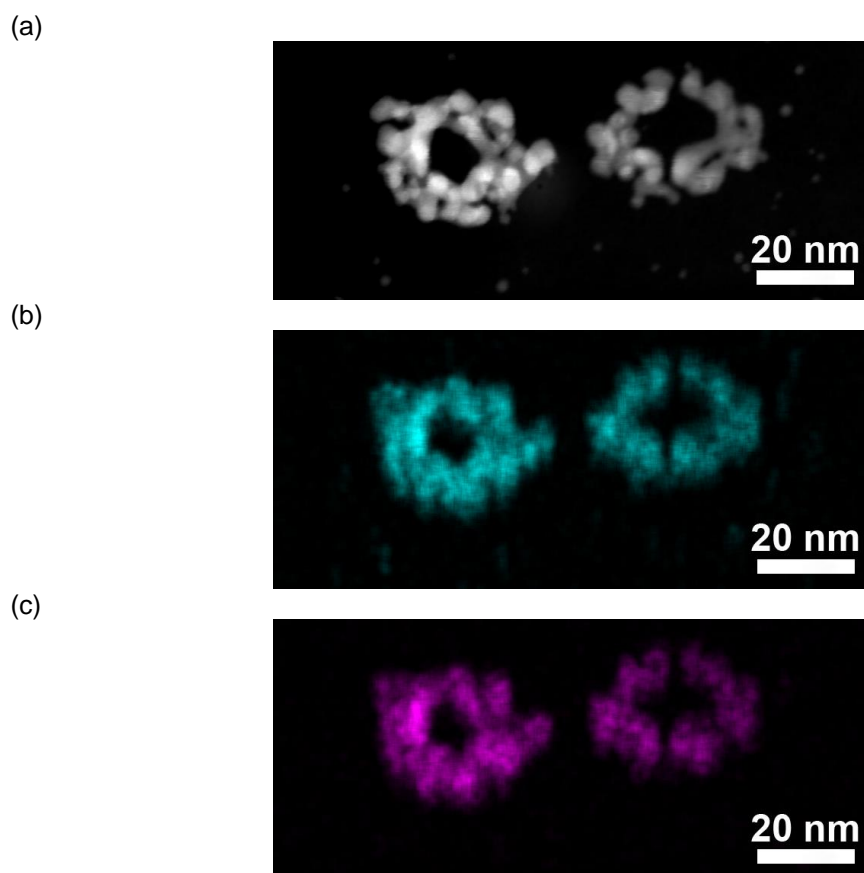
Figure S4. (a) HAADF TEM image of $Pt_{0.49}Au_{0.51}$ synthesized from PS_{1392}-*b*-$P4VP_{471}$. (b) Corresponding elemental map for Pt using the EDX signal from the Lα line (energy = 9.44 keV) for intensity. (c) Corresponding elemental map for Au using the EDX signal from the Lα line (energy = 9.71 keV) for intensity. The Pt:Au ratio was estimated as 45:55 by EDX.
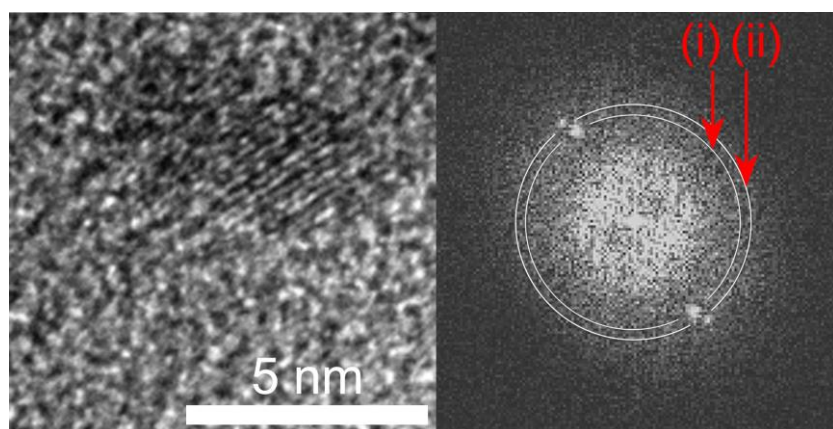
Figure S5. TEM image of $Pt_{0.61}Au_{0.39}$ synthesized from PS_{720}-*b*-$P4VP_{238}$ (left) and corresponding Fast-Fourier Transform (FFT) of this image (right). The Pt-rich shell is identified by intensity (ii) which corresponds to Pt (111). The intensity at (ii) corresponds to the Au-rich (111) core structure.

Figure S6. TEM image of $Pt_{0.41}Au_{0.59}$ synthesized from PS_{720}-*b*-$P4VP_{238}$ (left) and corresponding Fast-Fourier Transform (FFT) of this image (right). The Pt-rich shell is identified by intensity (ii) and (iv) which corresponds to Pt (111) and Pt (220), respectively. Intensities (i) and (iii) correspond to the Au-rich (111) and Au-rich (220) core structure, respectively.
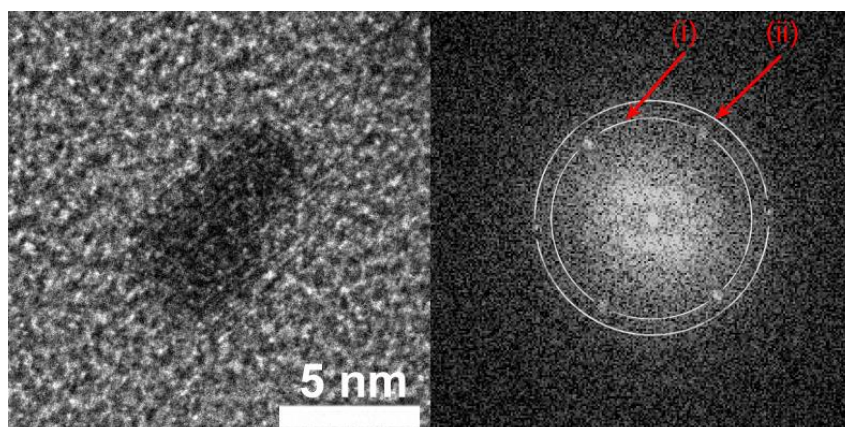
Figure S7. TEM image of $Pt_{0.49}Au_{0.51}$ synthesized from PS_{1392}-*b*-$P4VP_{471}$ (left) and corresponding Fast-Fourier Transform (FFT) of this image (right). The Pt-rich shell is identified by intensity (i) which corresponds to Pt (111). The intensity at (ii) corresponds to the Au-rich (200) core structure.
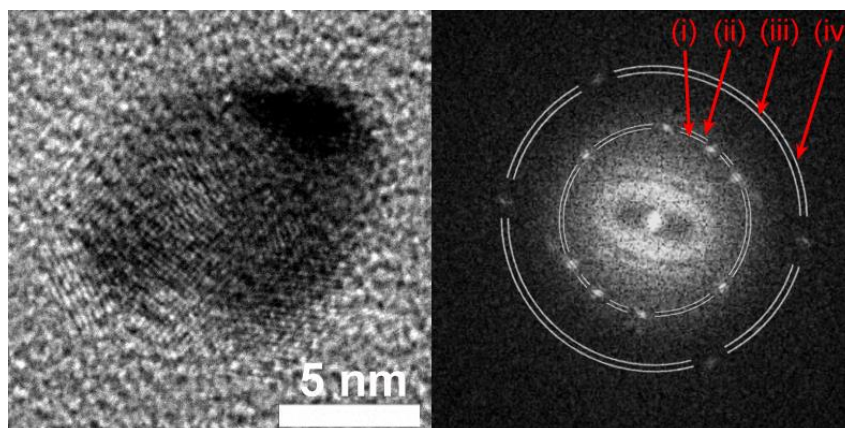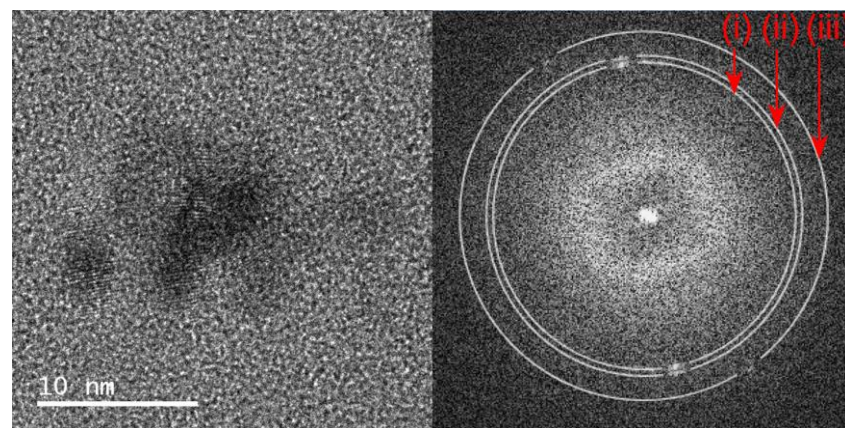

Figure S8. TEM image of $Pt_{0.61}Au_{0.39}$ synthesized from PS_{552}-*b*-$P4VP_{174}$ (left) and corresponding Fast-Fourier Transform (FFT) of this image (right). The Pt-rich shell is identified by intensity (ii)

which corresponds to Pt (111) where as (i) and (iii) correspond to the Au-rich (111) and Au-rich (200) core structure, respectively.
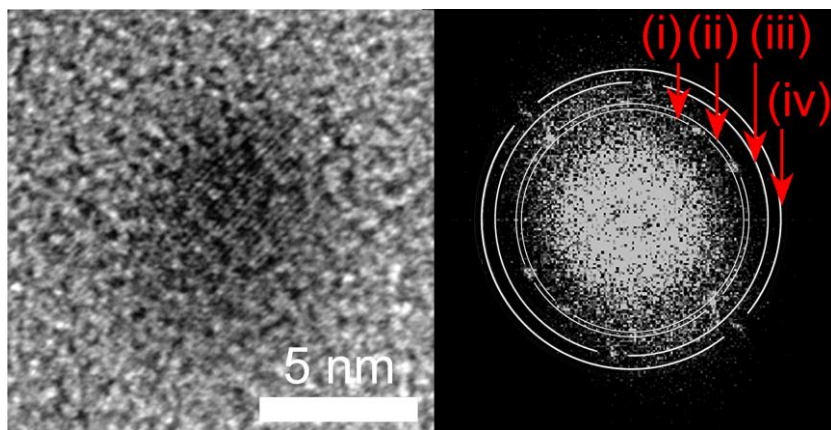
Figure S9. TEM image of $Pt_{0.61}Au_{0.39}$ synthesized from PS_{552}-*b*-$P4VP_{174}$ (left) and corresponding Fast-Fourier Transform (FFT) of this image (right). The Pt-rich shell is identified by intensity (ii) and (iv) which corresponds to Pt (111) and Pt (220), respectively. Intensities (i) and (iii) correspond to the Au-rich (111) and Au-rich (210) core structure, respectively.
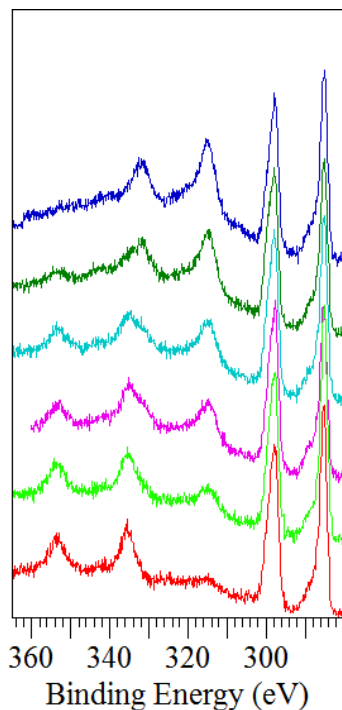

Figure S10. High-resolution XPS plots from PtAu NPs synthesized from PS_{1392}-*b*-$P4VP_{471}$. From top to bottom $Pt_{1.00}Au_{0.00}$, $Pt_{0.73}Au_{0.27}$, $Pt_{0.57}Au_{0.43}$, $Pt_{0.49}Au_{0.51}$, $Pt_{0.38}Au_{0.62}$ and $Pt_{0.00}Au_{1.00}$. The binding energies were corrected to the C 1s peak for the background hydrocarbon component (C–C/C–H_x) at 284.9 eV. The peak at 297.6 eV is the signal from the Magnesium source (Mg KLL).
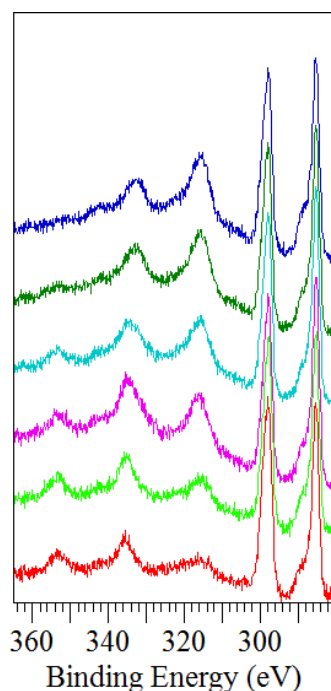
Figure S11. High-resolution XPS plots from PtAu NPs synthesized from PS_{720}-*b*-$P4VP_{238}$. From top to bottom $Pt_{1.00}Au_{0.00}$, $Pt_{0.72}Au_{0.28}$, $Pt_{0.61}Au_{0.39}$, $Pt_{0.56}Au_{0.44}$, $Pt_{0.41}Au_{0.59}$ and $Pt_{0.00}Au_{1.00}$. The binding energies were corrected to the C 1s peak for the background hydrocarbon component (C–C/C–H_x) at 284.9eV. The peak at 297.6 eV is the signal from the Magnesium source (Mg KLL).

Figure S12. High-resolution XPS plots from PtAu NPs synthesized from PS_{552}-*b*-$P4VP_{174}$. From top to bottom $Pt_{1.00}Au_{0.00}$, $Pt_{0.81}Au_{0.19}$, $Pt_{0.68}Au_{0.32}$, $Pt_{0.61}Au_{0.39}$, $Pt_{0.37}Au_{0.63}$ and $Pt_{0.00}Au_{1.00}$. The binding energies were corrected to the C 1s peak for the background hydrocarbon component (C–C/C–H_x) at 284.9eV. The peak at 297.6 eV is the signal from the Magnesium source (Mg KLL).
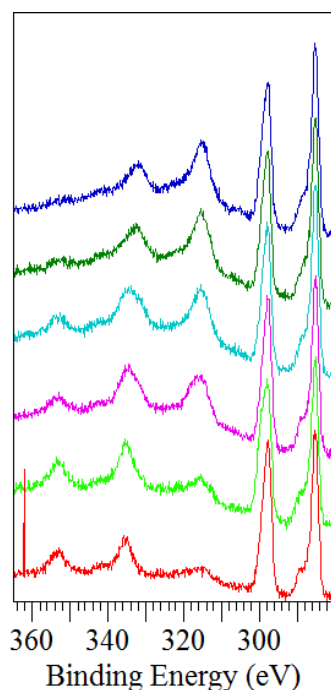
Table S1. Summary of 4d and 4f relative peak areas determined by curve fitting for PtAu NPs synthesized from PS_{1392}-b-$P4VP_{471}$.

	Pt 4d$_{5/2}$	Pt 4d$_{3/2}$	Au 4d$_{5/2}$	Au 4d$_{3/2}$	Pt 4f$_{5/2}$	Pt 4f$_{7/2}$	Au 4f$_{5/2}$	Au 4f$_{7/2}$
Pt$_{0.73}$Au$_{0.27}$	1389.2	930.8	527.0	353.1	893.7	670.3	253.3	190.0
Pt$_{0.57}$Au$_{0.43}$	1014.7	679.8	774.4	518.8	673.6	505.2	658.6	493.9
Pt$_{0.49}$Au$_{0.51}$	995.8	667.2	1011.4	677.6	650.1	487.6	968.4	726.3
Pt$_{0.38}$Au$_{0.62}$	613.1	410.8	1011.9	678.0	309.5	232.1	1112.2	834.1

Table S2. Summary of 4d peak relative areas determined by curve fitting for PtAu NPs synthesized from PS_{720}-b-$P4VP_{238}$.

	Pt 4d$_{5/2}$	Pt 4d$_{3/2}$	Au 4d$_{5/2}$	Au 4d$_{3/2}$
Pt$_{0.72}$Au$_{0.28}$	1089.3	729.8	426.9	286.0
Pt$_{0.61}$Au$_{0.39}$	809.9	542.7	513.9	344.3
Pt$_{0.56}$Au$_{0.44}$	666.9	446.8	526.5	352.8
Pt$_{0.41}$Au$_{0.59}$	369.2	247.4	526.3	352.6

Table S3. Summary of 4d peak relative areas determined by curve fitting for PtAu NPs synthesized from PS_{552}-b-$P4VP_{174}$.

	Pt 4d$_{5/2}$	Pt 4d$_{3/2}$	Au 4d$_{5/2}$	Au 4d$_{3/2}$
Pt$_{0.81}$Au$_{0.19}$	1486.9	996.3	347.2	232.6
Pt$_{0.68}$Au$_{0.32}$	1368.8	917.1	652.3	437.0
Pt$_{0.61}$Au$_{0.39}$	1213.4	813.0	777.3	520.8
Pt$_{0.37}$Au$_{0.63}$	620.3	415.6	1019.8	683.3

Table S4. Optimized conditions element specific detection by LA-ICP-MS.

__ICP-MS: Agilent 7500 CE__		__LA System: UP213__	
RF Torch Power	1550 W	laser energy	100% (~3.9 mJ)
Torch gas Flow (Ar)	1.22 L min^{-1}	laser frequency	10 Hz
cones	Ni skimmer, Ni sampler	laser diameter	55 µm
Isotope (abundance frac.)	^{118}Sn(0.242), ^{195}Pt(0.338)	ablation mode	10 samples within single line scan
sample integration time	0.1 s	scan speed	30 µm s^{-1}
__Substrate: Indium Tin Oxide: $(In_2O_3)_{0.9}(SnO_2)_{0.1}$__		acquisition length per sample	195 µm
Density, ρ (g/cm^3)	7.14	acquisition time per sample	6.5 s
Thickness (nm)	100	carrier gas flow rate (He)	0.6 L min^{-1}
atomic conc. Sn in ITO (%)	2.1		

The Pt-loading of Pt$_x$Au$_y$ bimetallic NPs produced from PS_n-b-$P4VP_m$ diblock copolymer templates on ITO can be estimated from laser-ablation inductively coupled plasma mass spectroscopy (LA ICP-MS, see Table S4 for experimental parameters) analysis. Pt quantification by the LA ICP-MS was conducted by relating signal intensity for ^{195}Pt to that of the ^{118}Sn

originating from the fully ablated ITO layer which is known to have constant composition and stoichiometry. Since the ITO substrate has a thickness of 100 nm and a composition of approximately 90 In_2O_3:10SnO_2,[1] the ^{118}Sn content of the substrate acts as a internal standard in the calculation. Table S5 reports the resulting estimates for Pt-loading per unit area for Pt_xAu_y bimetallic NPs produced from PS_n-b-$P4VP_m$ diblock copolymer templates.

Table S5. Dimensions, Stoichiometry and Pt-ECSA of Pt_xAu_y Bimetallic NPs produced from PS_n-b-$P4VP_m$ diblock copolymer template.

Bath Pt:Au mole ratio	Characteristic	Stoichiometry, ICP-MS signal intensity for ^{195}Pt and ^{118}Sn and resulting Pt-loading of Pt_xAu_y Bimetallic NPs produced from PS_n-b-$P4VP_m$ templates		
		PS_{1392}-b-$P4VP_{471}$	PS_{720}-b-$P4VP_{238}$	PS_{552}-b-$P4VP_{174}$
100:0	XPS-Estimated Composition	$Pt_{1.00}Au_{0.00}$	$Pt_{1.00}Au_{0.00}$	$Pt_{1.00}Au_{0.00}$
	10 sample ^{195}Pt Count (x 10^3)	26.1	138.7	219.8
	10 sample ^{118}Sn Count (x 10^3)	675.0	3513.3	4189.4
	Pt-loading (x 10^{-7} g/cm^2) [a]	3.03	3.10	4.11
98:2	XPS-Estimated Composition	$Pt_{0.73}Au_{0.27}$	$Pt_{0.72}Au_{0.28}$	$Pt_{0.81}Au_{0.19}$
	10 sample ^{195}Pt Count (x 10^3)	17.8	63.5	90.6
	10 sample ^{118}Sn Count (x 10^3)	501.5	1866.3	3109.1
	Pt-loading (x 10^{-7} g/cm^2) [a]	2.79	2.67	2.29
95:5	XPS-Estimated Composition	$Pt_{0.57}Au_{0.43}$	$Pt_{0.61}Au_{0.39}$	$Pt_{0.68}Au_{0.32}$
	10 sample ^{195}Pt Count (x 10^3)	22.2	60.0	78.1
	10 sample ^{118}Sn Count (x 10^3)	928.7	2779.4	2807.1
	Pt-loading (x 10^{-7} g/cm^2) [a]	1.88	1.69	2.18
88:12	XPS-Estimated Composition	$Pt_{0.49}Au_{0.51}$	$Pt_{0.56}Au_{0.44}$	$Pt_{0.61}Au_{0.39}$
	10 sample ^{195}Pt Count (x 10^3)	12.4	24.7	67.0
	10 sample ^{118}Sn Count (x 10^3)	545.2	1229.0	2569.5
	Pt-loading (x 10^{-7} g/cm^2) [a]	1.79	1.57	2.04

a - The mass loading of platinum was calculated relative to the signal generated for the ablated Sn from the well-defined ITO substrate. Complete ablation of the ITO layer (resting on float glass) beneath the Pt_xAu_y Bimetallic NPs catalyst layer was confirmed by monitoring the signals generated by the atomic constituents within the glass substrate (^{23}Na, ^{24}Mg, ^{27}Al, ^{28}Si, ^{29}Si, ^{43}Ca).

The moles of ^{118}Sn ablated during a single LA ICP-MS sample is:

$$= \frac{0.1 \, Vol. \, ITO_{ablated} \times \rho_{ITO}}{Molar \, Mass \, of \, ITO} \times (\text{fract. conc. Sn in ITO}) \times (\text{fract. abund. } ^{118}Sn)$$

The mass loading of platinum is:

$$= \frac{(\text{counts } ^{195}Pt)}{(fract. abund. \, ^{195}Pt)} \times \frac{(mol \, ^{118}Sn)}{(counts \, ^{118}Sn)} \times \frac{(Pt_{\text{Atomic Mass}})}{scan \, area}$$
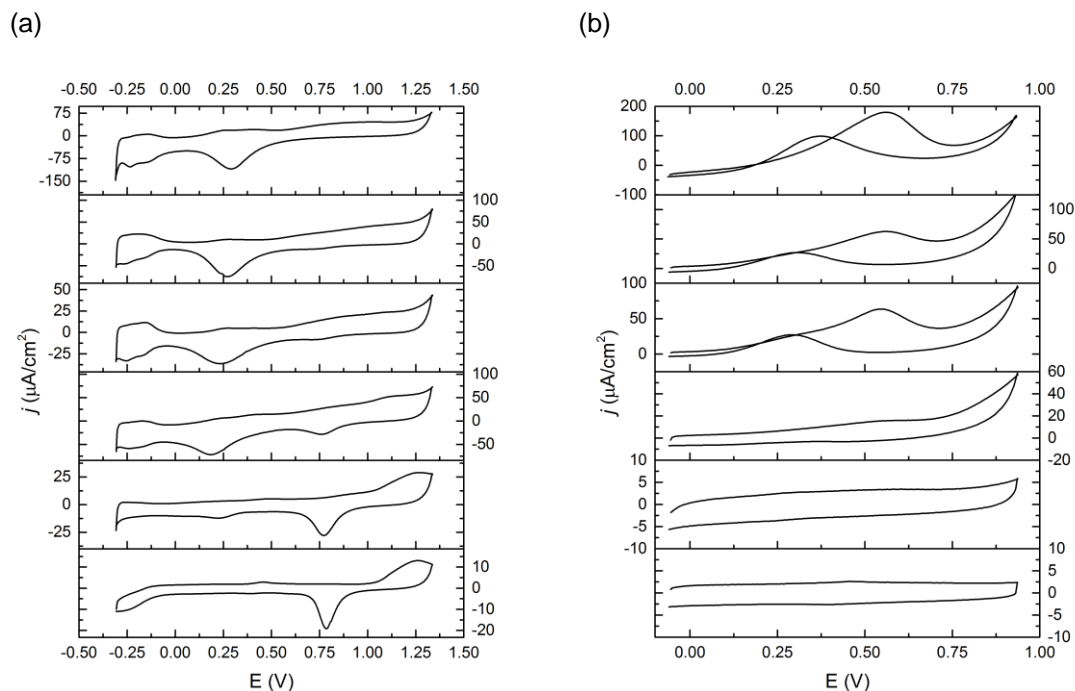
Figure S13. (a) Steady-state cyclic voltammetry plots (100 mV/sec, 0.1 M H_2SO_4) for PtAu NPs synthesized from PS_{1392}-*b*-$P4VP_{471}$. (b) Steady-state cyclic voltammetry plots (100 mV/sec, 0.1 M H_2SO_4; 2M MeOH) for methanol oxidation using PtAu NPs synthesized from PS_{1392}-*b*-$P4VP_{471}$. From top to bottom $Pt_{1.00}Au_{0.00}$, $Pt_{0.73}Au_{0.27}$, $Pt_{0.57}Au_{0.43}$, $Pt_{0.49}Au_{0.51}$, $Pt_{0.38}Au_{0.62}$ and $Pt_{0.00}Au_{1.00}$.
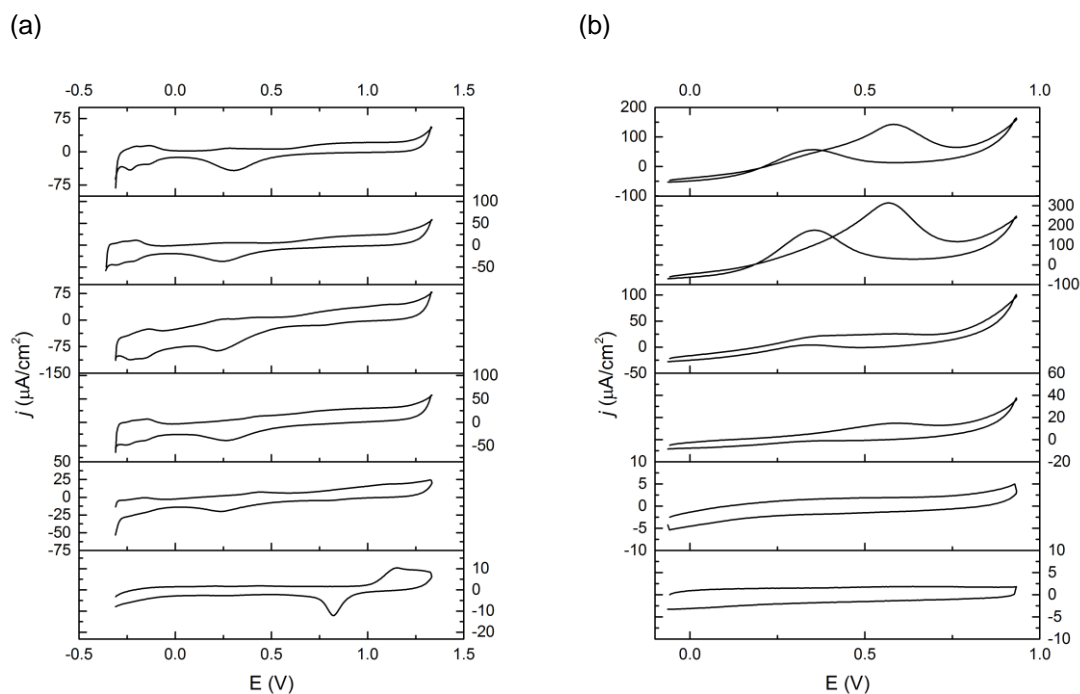

Figure S14. (a) Steady-state cyclic voltammetry plots (100 mV/sec, 0.1 M H_2SO_4) for PtAu NPs synthesized from PS_{720}-*b*-$P4VP_{238}$. (b) Steady-state cyclic voltammetry plots (100 mV/sec, 0.1 M H_2SO_4; 2M MeOH) for methanol oxidation using PtAu NPs synthesized from PS_{720}-*b*-$P4VP_{238}$. From top to bottom $Pt_{1.00}Au_{0.00}$, $Pt_{0.72}Au_{0.28}$, $Pt_{0.61}Au_{0.39}$, $Pt_{0.56}Au_{0.44}$, $Pt_{0.41}Au_{0.59}$ and $Pt_{0.00}Au_{1.00}$.
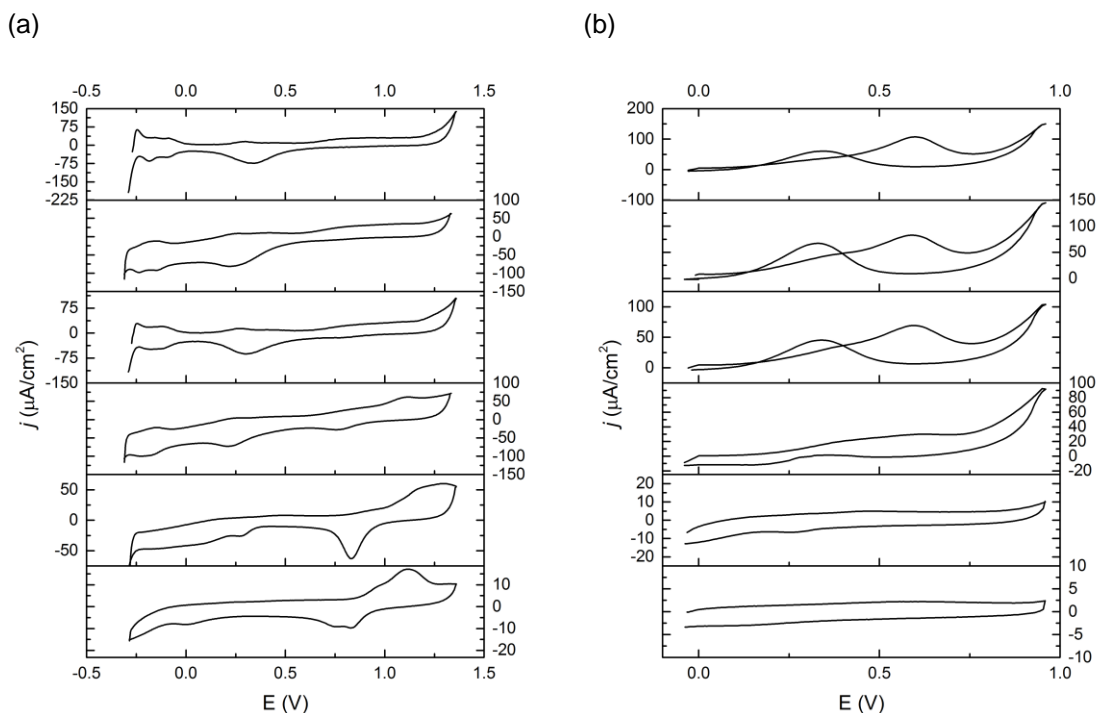
Figure S15. (a) Steady-state cyclic voltammetry plots (100 mV/sec, 0.1 M H_2SO_4) for PtAu NPs synthesized from PS_{552}-*b*-$P4VP_{174}$. (b) Steady-state cyclic voltammetry plots (100 mV/sec, 0.1 M H_2SO_4; 2M MeOH) for methanol oxidation using PtAu NPs synthesized from PS_{552}-*b*-$P4VP_{174}$. From top to bottom $Pt_{1.00}Au_{0.00}$, $Pt_{0.81}Au_{0.19}$, $Pt_{0.68}Au_{0.32}$, $Pt_{0.61}Au_{0.39}$, $Pt_{0.37}Au_{0.63}$ and $Pt_{0.00}Au_{1.00}$.

AFM and XPS analyses were used to confirm that samples prepared a polymer-overcasting and HF-etch procedure were similar in cluster definition and composition to those prepared directly on ITO electrodes (see Figure S16-S17 and Table S6-S7). The method involved transfer of the arrays of clusters of PtAu NPs to an ITO substrate from a floating polystyrene transfer layer created from relieving this layer from a sacrificial thermal oxide substrate (see experimental section). The transfer of a uniform and continuous PS layer bearing PtAu NPs onto the ITO substrate was complicated by the surface tension of the diluted $HF_{(aq)}$ and a drying artifact of the PS film. This affected the overall uniformity and density of the film but permitted enough material to be locally investigated by SFM and XPS. In the former, the dimensions for the periodicity and height of the array of PtAu NPs isolated from aurate and platinate loaded PS_{552}-*b*-$P4VP_{174}$ template created from the 88:12 Pt:Au immersion bath closely matched those in Table 1 (within 10%). In the latter, the overall signal for 4f electrons originating from the Pt and Au centers was less than that for a duplicate film prepared directly on ITO (without the floating and etching steps; see Figure S16). This reduced the overall signal to noise value which impacted the quality of the fit curves (see Figure S17). The values for the binding energies 4f electrons from Pt and Au for the fit curves and their areas are reported in Table S6 and S7, respectively. The approximate stoichiometry for PtAu NPs isolated from aurate and platinate loaded PS_{1392}-*b*-$P4VP_{471}$ template created from the direct route is $Pt_{0.41}Au_{0.59}$, an estimate that is with 10% of previously fabricated samples (see Table 2). The approximate stoichiometry for PtAu NPs isolated from aurate and platinate loaded PS_{1392}-*b*-$P4VP_{471}$ template created from the PS transfer route is $Pt_{0.54}Au_{0.46}$, an estimate that is with 10% of previously fabricated samples (see Table 2). Similarly, the agreement in the binding energies of 4f electrons from these two routes confirms that the overall oxidation state of the metals is similar in both cases (see Table S7).
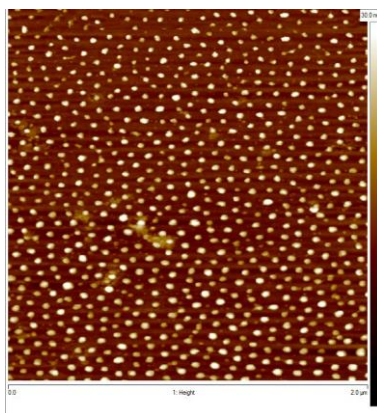
Figure S16. Scanning force microscopy (SFM) image of arrays of clusters of PtAu NPs isolated from aurate and platinate loaded PS$_{552}$-*b*-P4VP$_{174}$ template using the 88:12 Pt:Au immersion bath. Prior to SFM, the array was overcoated with a polystyrene (PS) layer and then floated to an air-water interface using HF and then captured on a silicon substrate for Ar plasma. The in-the-plane dimensions of the image are 2μm x 2μm. The height scale at right ranges from 0 to 30 nm.
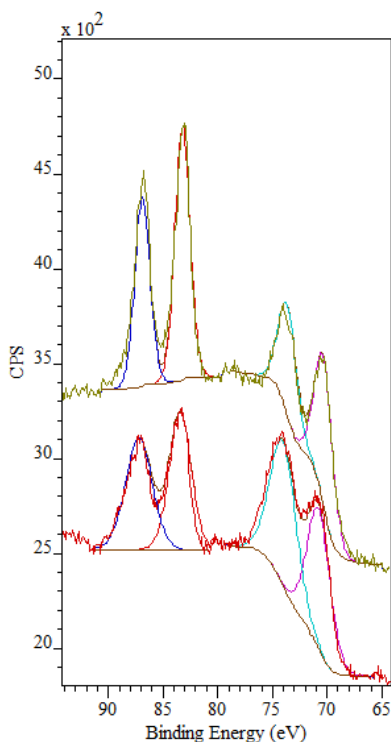

Figure S17. XPS comparison of ITO-supported arrays of clusters of PtAu NPs synthesized from PS$_{1392}$-*b*-P4VP$_{471}$ and the 88:12 platinate:aurate immersion bath isolated from direct preparation on an ITO substrate (top) and from preparation on silica substrate followed by embedding in polystyrene (PS) and transfer to ITO using HF and a final Ar plasma etch (see experimental section).

Table S6. Summary of binding energies of fitting curves from Figure S17 for 4f peaks for PtAu NPs synthesized from PS_{1392}-b-$P4VP_{471}$ and the 88:12 platinate:aurate immersion bath.

	Pt 4f$_{7/2}$ (eV)	Pt 4f$_{5/2}$ (eV)	Au 4f$_{7/2}$ (eV)	Au 4f$_{5/2}$ (eV)
PtAu NPs From direct isolation	86.9	83.2	73.6	70.3
PtAu NPs From PS transfer	87.1	83.4	74.1	70.6

Table S7. Summary of 4f peak relative areas determined by curve fitting from Figure S17 for PtAu NPs synthesized from PS_{1392}-b-$P4VP_{471}$ and the 88:12 platinate:aurate immersion bath.

	Pt 4f$_{7/2}$	Pt 4f$_{5/2}$	Au 4f$_{7/2}$	Au 4f$_{5/2}$
PtAu NPs From direct isolation	1620.4	1215.3	2346.2	1759.7
PtAu NPs From PS transfer	1981.3	2262.2	1852.6	1810.4

Reference:

1. *Delta Technologies, Product Information, www.delta-technologies.com.*